Global and Asymptotic stability analysis of open cavity flows

VINCENZO CITRO[1]†, FLAVIO GIANNETTI[1], LUCA BRANDT[2] AND PAOLO LUCHINI[1]

1 DIIN, University of Salerno, Via Giovanni Paolo II, 84084 Fisciano (SA), Italy

2 Linné Flow Centre and SeRC (Swedish e-Science Research Centre), KTH Mechanics, S-100 44 Stockholm, Sweden

(Received ?; revised ?; accepted ?. - To be entered by editorial office)

The viscous and inviscid linear stability of the incompressible flow past a square open cavity is studied numerically. The analysis shows that the flow first undergoes a pitchfork three-dimensional bifurcation at a critical Reynolds number of 1370. The critical mode is localized inside the cavity and has a flat roll structure with a spanwise wavelength of about 0.47 cavity depths. The adjoint global mode reveals that the instability is most efficiently triggered in the thin region close to the upstream tip of the cavity. The structural sensitivity analysis identifies the wavemaker as the region located inside the cavity and spatially concentrated around a closed orbit. As the flow outside the cavity plays no role on the generation mechanisms leading to the pitchfork bifurcation, we demonstrate that an appropriate parameter to describe the critical conditions in open cavity flows is the Reynolds number based on the average velocity between the two upper edges. Stabilization is achieved by a decrease of the total momentum inside the shear layer that drives the core vortex within the cavity. The mechanism of instability is then studied by means of a short-wavelength approximation (WKBJ) considering pressure-less inviscid modes. The closed streamline related to the maximum inviscid growth rate is found to be the same around which the global wave maker is concentrated. The structural sensitivity field based on direct and adjoint eigenmodes computed at a Reynolds number higher than that of the base flow, can predict the critical orbit providing the main contribution to the propagation of the three WKBJ instabilities. Further, we show that the sub-leading unstable time-dependent modes emerging at supercritical conditions are characterized by a period that is a multiple of the revolution time of Lagrangian particles along the orbit of maximum growth rate. The eigen-frequencies of these modes, computed by global stability analysis, are in very good agreement with the asymptotic results.

Key words: Open Cavity flows, Global Stability Analysis, Asymptotic Stability Analysis, Inviscid Structural Sensitivity

1. Introduction

Flow separation and recirculation are of great interest as they play an important role in the phenomena involving transport and mixing processes. The flow past open cavities is a prototype of geometrical configurations characterized by a finite region of separated flow. The identification of the flow characteristics (such as coherent structures) related to the instability mechanisms is also of practical importance since these may

† Email: vcitro@unisa.it

lead to resonance, acoustic noise or structural vibrations. Rockwell & Naudascher (1978) classified the unstable behavior of this kind of flows into fluid-dynamic, fluid-resonant, and fluid-elastic. Fluid-dynamic oscillations are due to the so-called *acoustic resonance* (Yamouni *et al.* 2013; Rossiter 1964): a feedback mechanism between the unstable shear layer susceptibile to Kelvin-Helmotz instability and pressure waves (Rowley *et al.* 2002). Fluid-resonant oscillations, on the contrary, are related to compressibility or free-surface wave phenomena whereas elastic oscillations are enhanced through elastic displacements of solid boundaries. Gharib & Roshko (1987) observed experimentally that the increase of the cavity length to depth ratio (L/D) led to a different kind of instability, the so-called "wake mode". This global instability relies on a purely hydrodynamic mechanism (the oscillation Strouhal number is weakly dependent on the Mach number) characterized by a large-scale vortex shedding (Rowley *et al.* 2002). The three-dimensional stability of compressible flow over open cavities has been recently investigated by Brés & Colonius (2008) for different geometrical aspect ratios (L/D). These authors found a steady mode of small spanwise wavelength for the square cavity and suggested that the linear instability is governed by a hydrodynamic mechanism.

Very recently, de Vicente *et al.* (2014) examined both experimentally and numerically the instabilities over a rectangular open cavity of aspect ratio $L/D = 2$. These authors compared the linear three-dimensional instability results with the spatial structure of the experimental fields showing qualitative agreement of the main flow properties. Furthermore, they also report that modifications of the spanwise boundary conditions can cause significant alterations of the flow field due to non-linear effects.

Instabilities in open and closed cavities as well as in separated flows, are interpreted as centrifugal instabilities. Centrifugal short-wave instabilities were first considered by Bayly (1988) who used the geometrical optics approximation and Flouquet theory to extend the classical Rayleigh theory for centrifugal instabilities to general inviscid planar flows. Bayly proposed to diagonalize the convective operator of the Linearized Euler equations (LEes) and construct linear asymptotic (WKBJ) eigenmodes, in the limit of large spanwise wavenumber, localized on the closed orbit characterized by the maximum Floquet exponent. Later, the same author showed qualitative agreement between the results obtained with the linearized Navier Stokes equations and the asymptotic predictions (Bayly 1989). Lifschitz & Hameiri (1991) investigated the asymptotic instabilities features considering the initial value problem for the LEes and for the linearized equations of gas dynamics. Their more general approach was able to include both exponential and algebraic growth in time. Many efforts have since been made to quantitatively link the short-wave asymptotics and the normal mode analysis: Sipp *et al.* (1999) showed agreement between the *optimal* streamline (i.e. the streamline where the inviscid growth rate is maximum) and the spatial distribution of the unstable eigenmodes, and between the inviscid and viscous amplification rate of an elliptic instability. Gallaire *et al.* (2007) examined the centrifugal instability of the separated region behind a bump and were able to make a composite estimation of the growth rate taking into account the viscous effects (see also Landman & Saffman 1987) and the short-wave inviscid asymptotic limit.

In this context, the main goal of the present work is to characterize the instabilities of the flow past an open cavity, develop an asymptotic approach to understand the instability mechanisms and finally relate the results of the global and local aymptotic analysis. The specific questions we shall answer, defining the outline of the article, are:

i) Provide an accurate estimation of the critical Reynolds number and the spanwise wavenumber of the first three-dimensional bifurcation in incompressible open cavity flows;

ii) Determine the *instability core* by means of the adjoint-based structural sensitivity analysis;

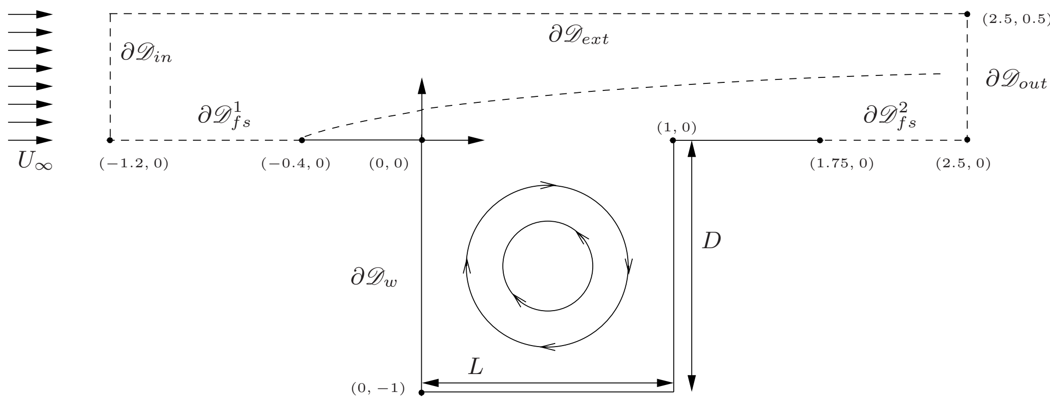

FIGURE 1. Flow configuration, frame of reference and computational domain $\mathscr{D}$. The main features of the flow are also sketched in the figure, i.e. the boundary layer developing over the walls, the shear layer above the cavity and the recirculation forming inside the cavity of length L and depth $D = L$.

iii) Identify the relevant parameters associated with the critical conditions, i.e. the identification of a convenient length scale and reference velocity;

iv) Investigate the sensitivity of the leading instability to base flow modifications induced by a perturbation of the inflow profile or wall blowing/suction;

v) Provide a quantitative prediction of the onset of the instability by means of the short-wave asymptotic theory;

vi) Show that the *inviscid* structural sensitivity (i.e. structural sensitivity based on direct and adjoint eigenmode computed at a Reynolds number higher than that of the base flow) is able to accurately predict the particle orbit that provides the main contribution to the instability.

vii) Suggest a generalization of the expression used to calculate the instability growth rate from the Floquet exponent to predict the frequency of the time-dependent modes emerging at supercritical conditions.

2. Theoretical Framework

2.1. *Geometrical configuration and Base flow*

We investigate the stability and sensitivity of the flow over a spanwise-uniform square open cavity exposed to a uniform stream. The geometry, the frame of reference and the notation adopted in this work are all displayed in figure 1. The origin of the Cartesian reference system is located on the left edge of the cavity with x, y and z denoting the streamwise, wall-normal and spanwise directions. The fluid motion is described by the unsteady incompressible Navier-Stokes equations,

$$\boldsymbol{\nabla} \cdot \boldsymbol{u} = 0, \tag{2.1a}$$

$$\frac{\partial \boldsymbol{u}}{\partial t} + (\boldsymbol{u} \cdot \boldsymbol{\nabla})\boldsymbol{u} = -\boldsymbol{\nabla} P + \frac{1}{Re_{\mathcal{BF}}} \boldsymbol{\nabla}^2 \boldsymbol{u}, \tag{2.1b}$$

where $\boldsymbol{u}$ is the velocity vector with components $\boldsymbol{u} = (u, v, w)$ and P is the reduced pressure. Equations (2.1) are made dimensionless using the cavity depth D as the characteristic length scale and the velocity of the incoming uniform stream U_∞ as the reference velocity. The Reynolds number is thus defined as $Re_{\mathcal{BF}} = U_\infty D/\nu$ (here the subscript $\mathcal{BF}$ means Base flow Reynolds number) with ν the fluid kinematic viscosity. To ease comparisons, we have chosen the same boundary conditions as Sipp & Lebedev (2007) and Barbagallo *et al.* (2009). The system of differential equations (2.1) is closed by the following Dirichlet boundary conditions at the inflow $\partial\mathscr{D}_{in}$ and stress-free conditions at the outflow $\partial\mathscr{D}_{out}$:

$$\boldsymbol{u} = 1 \cdot \boldsymbol{e}_x, \quad x \in \partial\mathscr{D}_{in}; \qquad P\boldsymbol{n} - Re^{-1}(\boldsymbol{\nabla u}) \cdot \boldsymbol{n} = \boldsymbol{0}, \quad x \in \partial\mathscr{D}_{out}.$$

Symmetric conditions (i.e. $\partial_y u = 0$ and $v = 0$) are imposed at the free-stream upper boundary of the computational domain $\partial\mathscr{D}_{ext}$ and no-slip conditions $\boldsymbol{u} = \boldsymbol{0}$ at the solid walls $\partial\mathscr{D}_w$. Note that a free-slip condition with zero tangential stress (i.e. $\partial_y u = 0$ and $v = 0$) is used on the walls close to the inflow and outflow $\partial\mathscr{D}_{fs} = \partial\mathscr{D}^1_{fs} \cup \partial\mathscr{D}^2_{fs}$.

2.2. *Global stability analysis*

The flow linear instability is studied with a classical normal-mode analysis. The analysis relies on the existence of a steady solution about which infinitesimal perturbations are superimposed. The velocity and pressure fields are decomposed into a two-dimensional base flow, $\boldsymbol{Q_b}(x, y) = (\boldsymbol{u}_b, P_b)^T = (u_b, v_b, 0, P_b)^T$, and a three-dimensional disturbance flow denoted by $\boldsymbol{q'}(x, y, z, t) = (\boldsymbol{u}', P')^T = (u', v', w', P')^T$ of small amplitude ϵ. Introducing this decomposition into equations (2.1) and linearizing the equations governing the disturbance evolution, we obtain the two systems describing the spatial structure of the base flow and the behavior of generally unsteady perturbations. In particular, the base flow is governed by the steady version of (2.1), whereas the perturbation field is described by the linearized unsteady Navier-Stokes equations (LNSE)

$$\frac{\partial \boldsymbol{u}'}{\partial t} + \boldsymbol{L}\{\boldsymbol{u}_b(Re_{\mathcal{BF}}), Re_{\mathcal{STB}}\}\boldsymbol{u}' = -\boldsymbol{\nabla} P', \tag{2.2}$$

$$\nabla \cdot \boldsymbol{u}' = 0, \tag{2.3}$$

with the linearized Navier-Stokes operator $\boldsymbol{L}$ ($Re_{\mathcal{STB}}$ indicates the Reynolds number used for stability computations)

$$\boldsymbol{L}\{\boldsymbol{u}_b, Re_{\mathcal{STB}}\}\boldsymbol{u}' = \boldsymbol{u}_b \cdot \boldsymbol{\nabla u}' + \boldsymbol{u}' \cdot \boldsymbol{\nabla u}_b - \frac{1}{Re_{\mathcal{STB}}}\boldsymbol{\nabla}^2\boldsymbol{u}'. \tag{2.4}$$

As the base flow is homogeneous and stationary in the spanwise direction, a generic perturbation can be decomposed into Fourier modes of spanwise wavenumber k. The three-dimensional perturbations are expressed as

$$\boldsymbol{q}'(x, y, z, t) = \frac{1}{2}\{(\hat{u}, \hat{v}, \hat{w}, \hat{P})(x, y)\ exp[ikz + \gamma t] + c.c.\}, \tag{2.5}$$

where $\gamma = \eta + i\omega$ is the complex growth rate and *c.c.* stands for complex conjugate. The real part η of γ represents the temporal growth rate of the perturbation and the imaginary part ω its frequency. For $\eta > 0$, the flow is unstable whereas for $\eta < 0$ it is stable. Introducing the ansatz (2.5) in the LNSE (2.2-2.3), we obtain the generalized eigenvalue problem

$$\mathscr{A}\hat{\mathbf{q}} + \gamma\mathscr{B}\hat{\mathbf{q}} = 0, \tag{2.6}$$

in which $\hat{\mathbf{q}} = (\hat{u}, \hat{v}, \hat{w}, \hat{P})^T$ and $\mathscr{A}$ is the complex linearized evolution operator. The operators $\mathscr{A}$ and $\mathscr{B}$, have the following expression

$$\mathscr{A} = \begin{pmatrix} \mathscr{C} - \mathscr{M} + \partial_x u_b & \partial_y u_b & 0 & \partial_x \\ \partial_x v_b & \mathscr{C} - \mathscr{M} + \partial_y v_b & 0 & \partial_y \\ 0 & 0 & \mathscr{C} - \mathscr{M} & ik \\ \partial_x & \partial_y & ik & 0 \end{pmatrix}, \quad \mathscr{B} = \begin{pmatrix} 1 & 0 & 0 & 0 \\ 0 & 1 & 0 & 0 \\ 0 & 0 & 1 & 0 \\ 0 & 0 & 0 & 0 \end{pmatrix}, \tag{2.7}$$

where $\mathscr{M} = {Re_{\mathcal{STB}}}^{-1}(\partial_{x^2}+\partial_{y^2}-k^2)$ and $\mathscr{C} = u_b\partial_x + v_b\partial_y$ describe the viscous diffusion of the perturbation and its advection by the mean flow. The boundary conditions associated with the eigenproblem (2.6) are derived from those used for the base flow, i.e.

$$\hat{\boldsymbol{u}} = \boldsymbol{0}, \text{ on } \partial\mathscr{D}_{in} \cup \partial\mathscr{D}_w \text{ (inlet and wall)}, \tag{2.8a}$$

$$\hat{P}\boldsymbol{n} - {Re_{\mathcal{STB}}}^{-1}(\boldsymbol{\nabla}\hat{\mathbf{u}}) \cdot \boldsymbol{n} = \boldsymbol{0}, \text{ on } \partial\mathscr{D}_{out} \text{ (outlet)}, \tag{2.8b}$$

$$\partial_y \hat{u} = \hat{v} = \hat{w} = 0, \text{ on } \partial\mathscr{D}_{ext} \cup \partial\mathscr{D}_{fs} \text{ (free stream and free-slip boundary)}. \tag{2.8c}$$

Finally, we note that the complex conjugate pairs $(\eta + i\omega; \hat{\mathbf{q}})$ and $(\eta - i\omega; \hat{\mathbf{q}}^*)$ are both solution of the eigenproblem (2.6) with the boundary conditions (2.8) for a real base flow $\boldsymbol{Q_b}$. Thus, the eigenvalues are complex conjugates and the spectra is symmetric plane with respect to the real axis in the (η, ω).

2.3. *Determination of the instability core: structural sensitivity*

In this section we present the structural sensitivity analysis following the framework in Pralits *et al.* (2010). The underlying idea is the concept of "wavemaker", introduced by Giannetti & Luchini (2007) to identify the location of the core of a global instability. The wavemaker is the region in the flow where variations in the structure of the problem provide the largest drift of a specific eigenvalue. We first consider the perturbed eigenvalue problem

$$\gamma' \hat{\boldsymbol{u}}' + \boldsymbol{L}\{\boldsymbol{u}_b, Re_{\mathcal{STB}}\}\hat{\boldsymbol{u}}' = -\boldsymbol{\nabla}\hat{P}' + \delta\boldsymbol{H}(\hat{\boldsymbol{u}}', \hat{P}'), \tag{2.9}$$

$$\nabla \cdot \hat{\boldsymbol{u}}' = 0, \tag{2.10}$$

where $\delta\boldsymbol{H}$ is the generalized structural perturbation. It is assumed to be a momentum force localized in space and proportional to the local velocity perturbation through a (3×3) coupling matrix $\delta\boldsymbol{M}_0$ and a Dirac delta function

$$\delta\boldsymbol{H}(\hat{\boldsymbol{u}}', \hat{P}') = \delta\boldsymbol{M}(x, y) \cdot \hat{\boldsymbol{u}}' = \delta(x - x_0, y - y_0)\delta\boldsymbol{M}_0 \cdot \hat{\boldsymbol{u}}'. \tag{2.11}$$

Neglecting higher order terms, variations of the eigenvalue $\delta\gamma$ and of the corresponding eigenfunction $(\delta\hat{\boldsymbol{u}}, \delta\hat{P})$ satisfy the following expression

$$\gamma\delta\hat{\boldsymbol{u}} + \boldsymbol{L}\{\boldsymbol{u}_b, Re_{\mathcal{STB}}\}\delta\hat{\boldsymbol{u}} = -\boldsymbol{\nabla}\delta\hat{P} + \delta\boldsymbol{M} \cdot \hat{\boldsymbol{u}} - \delta\gamma\hat{\boldsymbol{u}}, \tag{2.12}$$

$$\boldsymbol{\nabla} \cdot \delta\hat{\boldsymbol{u}} = 0. \tag{2.13}$$

Using then the Lagrange identity (see Luchini & Bottaro 2014), we can determine the equations governing the structure of the adjoint field $\hat{\boldsymbol{g}}^+(x, y) = (\hat{\boldsymbol{f}}^+, \hat{m}^+)$

$$-\gamma\hat{\boldsymbol{f}}^+ + \boldsymbol{u}_b \cdot \boldsymbol{\nabla}\hat{\boldsymbol{f}}^+ - \boldsymbol{\nabla}\boldsymbol{u}_b \cdot \hat{\boldsymbol{f}}^+ + \frac{1}{Re_{\mathcal{STB}}}\boldsymbol{\nabla}^2\hat{\boldsymbol{f}}^+ + \boldsymbol{\nabla}\hat{m}^+ = 0, \tag{2.14}$$

$$\boldsymbol{\nabla} \cdot \hat{\boldsymbol{f}}^+ = 0. \tag{2.15}$$

After integration over the domain $\mathscr{D}$, accounting for the boundary conditions and introducing the sensitivity tensor

$$\boldsymbol{S}(x_0, y_0; Re_{\mathcal{BF}}, Re_{\mathcal{STB}}) = \frac{\hat{\boldsymbol{f}}^{+}(x_0, y_0)\hat{\boldsymbol{u}}(x_0, y_0)}{\int_{\mathscr{D}} \hat{\boldsymbol{f}}^{+} \boldsymbol{\cdot} \hat{\boldsymbol{u}} dS}, \tag{2.16}$$

we can express the eigenvalue drift due to the local feedback as

$$\delta\gamma(x_0, y_0) = \frac{\int_{\mathscr{D}} \hat{\boldsymbol{f}}^{+} \boldsymbol{\cdot} \delta\boldsymbol{M} \boldsymbol{\cdot} \hat{\boldsymbol{u}} dS}{\int_{\mathscr{D}} \hat{\boldsymbol{f}}^{+} \boldsymbol{\cdot} \hat{\boldsymbol{u}} dS} = \frac{\hat{\boldsymbol{f}}^{+} \boldsymbol{\cdot} \delta\boldsymbol{M}_0 \boldsymbol{\cdot} \hat{\boldsymbol{u}}}{\int_{\mathscr{D}} \hat{\boldsymbol{f}}^{+} \boldsymbol{\cdot} \hat{\boldsymbol{u}} dS} = \boldsymbol{S} : \delta\boldsymbol{M}_0 = \sum_{ij} S_{ij} \delta M_{0ij}. \tag{2.17}$$

Different norms of the tensor $\boldsymbol{S}$ can be used to build a spatial map of the sensitivity. The spectral norm is chosen here to study the worst possible case.

3. Numerical approach

3.1. *Base flow calculation*

The numerical computation of the base flow has been performed using a finite element method. The variational formulation of the Navier-Stokes equations (2.1) is implemented in the software package FreeFem++ (http://www.freefem.org) using classical $P2-P1$ Taylor-Hood elements for the spatial discretization. The resultant nonlinear system of algebraic equations, along with the boundary conditions, is solved by a Newton-Raphson procedure: given an initial guess $\mathbf{w}_b{}^{(0)}$, the linear system

$$\mathbf{NS}(Re_{\mathcal{BF}}, \mathbf{W}_b{}^{(n)}) \cdot \mathbf{w}_b{}^{(n)} = -\mathbf{rhs}^{(n)} \tag{3.1}$$

is solved at each iteration step using the MUMPS-Multifrontal Massively Parallel sparse direct Solver (Amestoy *et al.* 2001, 2006) for the matrix inversion. The base flow is then updated as

$$\mathbf{W}_b{}^{(n+1)} = \mathbf{W}_b{}^{(n)} + \mathbf{w}_b{}^{(n)}. \tag{3.2}$$

The initial guess is chosen to be the solution of the Stokes equations and the process is continued until the L^2-norm of the residual of the governing equations becomes smaller than 10^{-12}. To test the implementation and convergence, we used three different meshes $\mathcal{M}\mathbf{1}$, $\mathcal{M}\mathbf{2}$ and $\mathcal{M}\mathbf{3}$ (see Table 1). These are generated by the Bidimensional Anisotropic Mesh Generator (Bamg) that is part of the Freefem++ package. The base flow computations are also validated using a variant of the second-order finite-difference code described in Giannetti & Luchini (2007). A typical steady flow over the open cavity is depicted in figure 2.

3.2. *Eigenvalue solver and adjoint field*

Once the base flow is determined, the system of equations (2.6) is used to perform the stability analysis. After spatial discretization, the governing equations and their boundary conditions (2.8) are recast in the following standard form

$$[\mathbf{A}(Re_{\mathcal{STB}}, \mathbf{W}_b(Re_{\mathcal{BF}})) + \gamma\mathbf{B}] \cdot \mathbf{w} = \mathbf{0}, \tag{3.3}$$

where $\mathbf{w}$ is the right (or direct) eigenvector. As methods based on the QR decomposition are not feasible for solving large scale problems as those associated to the matrix $\mathbf{A}$ obtained for our problem, we adopt an efficient matrix-free iterative method based on the Arnoldi algorithm (Arnoldi 1951). We use the state-of-the-art ARPACK package (Lehoucq *et al.* 2007), with implicit restarts to limit memory requirements. The solution of the linear system built by the Arnoldi iterations on the Krylov subspace is obtained

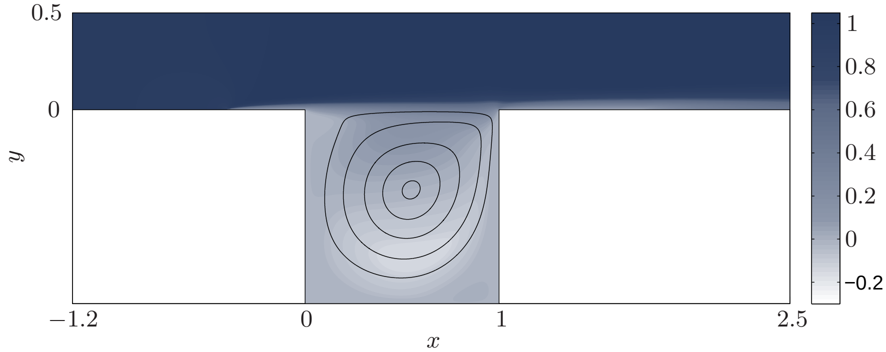

FIGURE 2. Visualisation of the steady two-dimensional base flow for the Reynolds number $Re_{\mathcal{BF}} = 1370$ at which a three-dimensional instability is first observed. The background color displays the streamwise velocity whereas solid lines indicate the streamlines inside the cavity.

Mesh	η	ω	$n_{d.o.f.}$	n_t	Source
$\mathcal{M}\mathbf{1}$	0.0007590	7.4931	998668	221045	Present
$\mathcal{M}\mathbf{2}$	0.0008344	7.4937	1416630	313791	Present
$\mathcal{M}\mathbf{3}$	0.0009122	7.4943	2601757	576887	Present
$\mathcal{D}\mathbf{1}$	0.0007401	7.4930	880495	194771	Sipp & Lebedev (2007)
$\mathcal{D}\mathbf{2}$	0.0008961	7.4942	1888003	418330	Sipp & Lebedev (2007)

TABLE 1. Comparison of the results obtained with the present implementation and those reported by Sipp & Lebedev (2007) for the same configuration. The eigenfrequency ω and the growth rate η have been calculated for the first two-dimensional unstable eigenmode at $Re_{\mathcal{BF}} = Re_{\mathcal{STB}} = 4140$. $n_{d.o.f.}$ and n_t indicate the total number of degrees of freedom of the linearized problem and the number of triangles for each of the unstructured meshes used.

with the same sparse solver (Amestoy *et al.* 2001, 2006) used for the base flow calculations. The adjoint modes are computed as left eigenvectors of the discrete system derived from the discretization of the linearized equations and the sensitivity function is then computed by the product of the direct and the adjoint fields. The right (direct) and left (adjoint) eigenvectors are normalized by requiring

$$\max_{x,y\in\mathscr{D}}\{|\hat{u}(x,y)|\} = 1, \quad \int_{\mathscr{D}} \hat{\boldsymbol{f}}^{+} \cdot \hat{\boldsymbol{u}}\, dS = 1. \tag{3.4}$$

The code is validated against the results reported by Sipp & Lebedev (2007). These authors investigate the stability of a newtonian fluid in the same geometrical configuration and report the first instability of a two-dimensional eigenmode to occur at Re=4140. In Table 1 we present the comparison between our results and the results in Sipp & Lebedev (2007) for different meshes. In these tests, 50 eigenvalues were obtained, with an initial Krylov basis of dimension 150; the convergence criterion for the Arnoldi iterations is based on a tolerance of 10^{-9}. To independently check the accuracy of the results we *a posteriori* computed the residual $max_i|(A_{ij}+\gamma B_{ij})w_j|$: this turns out to be always below 10^{-9} for the results reported in this paper, typically less than 10^{-12} for the least stable modes. The majority of the computations presented in the following are obtained using mesh $\mathcal{M}\mathbf{2}$. Henceforth whenever $Re_{\mathcal{BF}} = Re_{\mathcal{STB}}$ we will simply use Re.

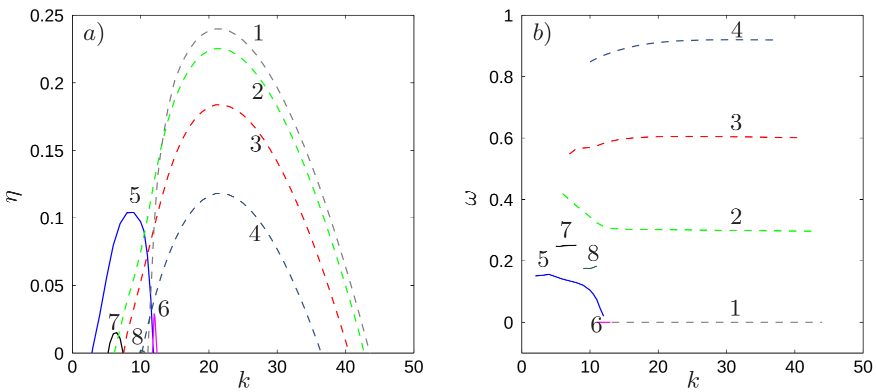

FIGURE 3. Stability analysis of the open-cavity flow at $Re = 4140$, where an unstable two-dimensional mode first emerge. a) Real and b) immaginary part of the eigenvalue γ versus the spanwise wavenumber k. The different branches are numerated for future reference.

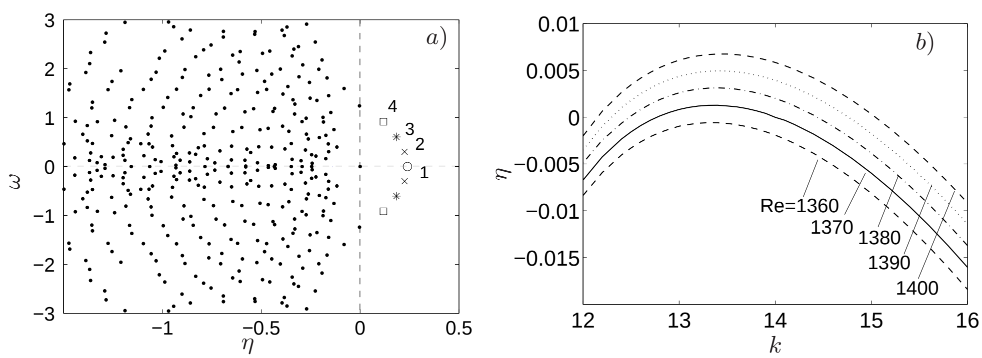

FIGURE 4. a) Eigenvalue spectrum for $Re = 4140$ and $k = 22$. The numbers in the figure relates to the branches identified in figure 3. b) Growth rate of the least unstable mode versus the span wise wavenumber k for the Reynolds indicated. The circular frequency is zero for all modes displayed. The first instability of the flow over an open cavity is a three-dimensional steady mode.

4. Linear stability results

4.1. *Three-dimensional vs. two-dimensional instability*

As the cavity is typically considered an example of centrifugal instability, we expect the first bifurcation to be characterized by the appearance of steady three-dimensional modes of relatively short wavelength in the spanwise direction (Albensoeder *et al.* 2001). To verify this, we scan the k-axis seeking for unstable modes at the Reynolds number $Re = 4140$ where a two-dimensional mode first become unstable (Sipp & Lebedev 2007). The results in figure 3 clearly show that 8 unstable branches can be found for this value of Re where the most unstable mode has wavenumber $k = 22$ and represents a steady disturbance ($\omega = 0$ in figure 3b). The flow over an open-cavity is therefore characterized by a first bifurcation to a steady three-dimensional configuration.

The full eigenvalue spectrum at $k = 22$ is shown in figure 4a) where 7 unstable modes appear (4 branches), placed symmetrically with respect to the real axis. It is interesting to note that the steady mode is the most unstable and the other branches appear as *harmonics* of the global mode denoted as 2 in the plot.

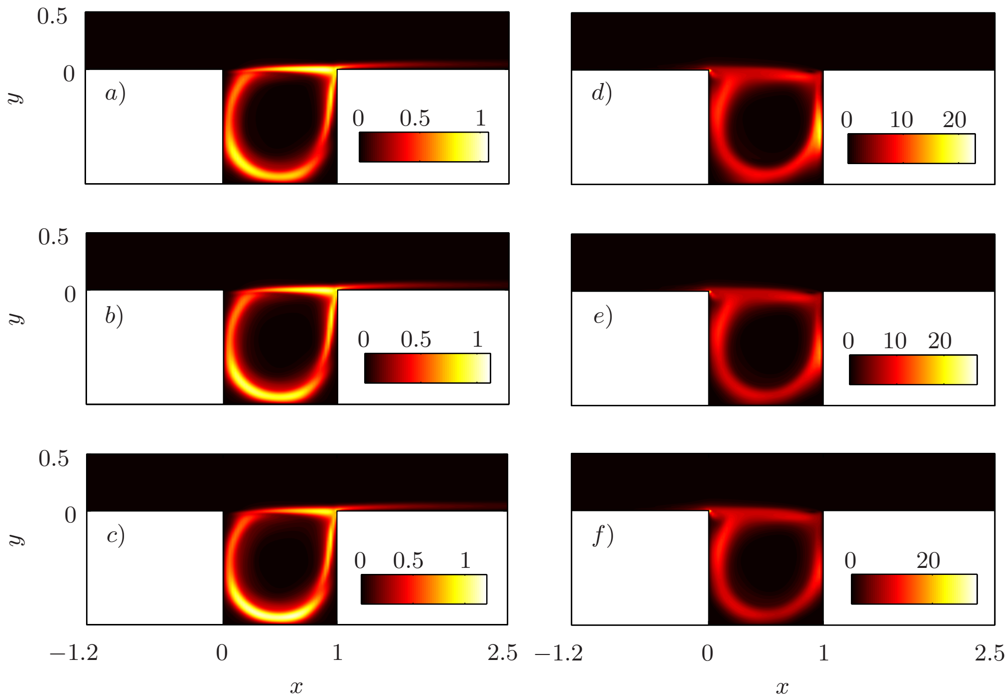

FIGURE 5. Contour plots of the absolute value of the direct and adjoint eigenfunctions of modes 2,3 and 4 as denoted in figure 4a) for $Re = 4140$ and $k = 22$. a) and d): direct and adjoint of mode 2 ($\omega \approx 0.3$); b) and e) mode 3 ($\omega \approx 0.6$); c) and f) mode 4 ($\omega \approx 0.9$).

To document the appearance of this two-to-three-dimensional bifurcation, we determine the critical Reynolds number at which the instability first occurs: as shown in figure 4(b) the critical value is about $Re_{cr} \approx 1370$ and the first mode to become unstable is associated to a wavenumber $k \approx 13.4$. All modes whose growth rate is reported in the figure have zero frequency and we are therefore in the presence of a pitchfork bifurcation to a steady spanwise modulated flow. This instability will be analyzed in detail in the rest of the paper.

In figure 5 we display the modulus of both the direct and adjoint eigenfunctions corresponding to the eigenvalues denoted by 2, 3, and 4 in figure 4a). The velocity perturbations are most evident in the circular region inside the cavity, with a tail on the shear region just above the downstream wall. The adjoint modes, indicating the region in the flow most receptive to forcing in the momentum equations, have a similar structure, except for the thin region close to the upstream tip of the cavity, where instability is most efficiently triggered. The unstable modes are spatially localized in the same region. The secondary flow generated by the leading instability can be described as a flat roll lying within the square cavity. The higher harmonics are associated to periodic oscillations again concentrated in the region inside the cavity.

4.2. *Structural sensitivity of the first bifurcation*

We study the characteristics of the bifurcation by first showing the spatial structure of the fluctuation of the least stable mode at $Re = 1370$, $k = 13.4$. As for the modes at higher Reynolds number, the mode is localized along the external streamlines of the

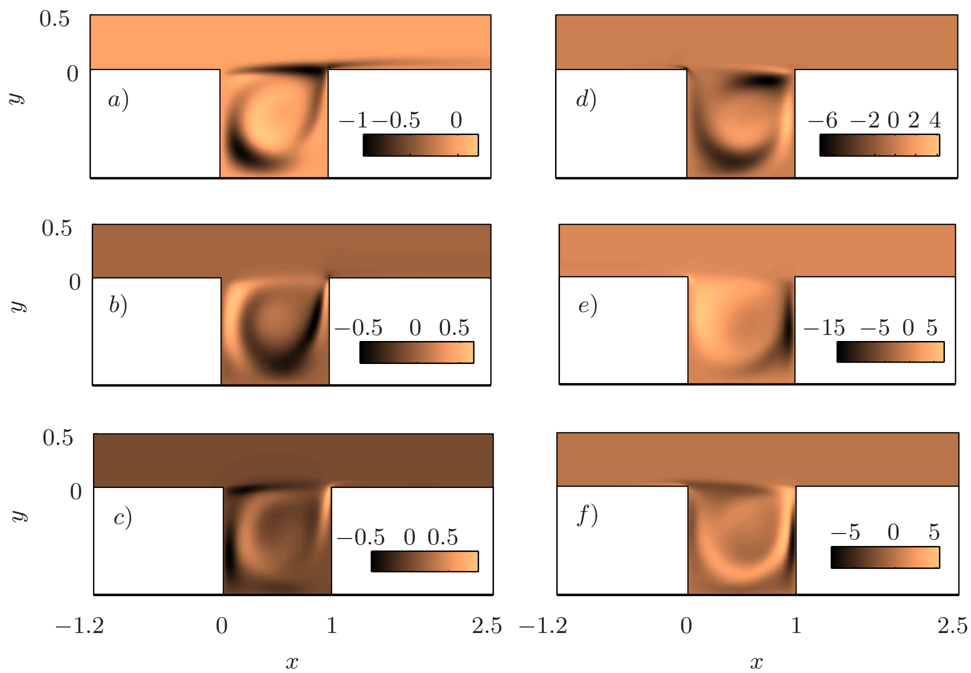

FIGURE 6. Contour plots of the streamwise (a-direct; d-adjoint), wall-normal (b-direct; e-adjoint) and spanwise (c-direct; f-adjoint) component of the direct and adjoint mode close to the critical Reynolds number $Re = 1370$, $k = 13.4$.

recirculation region inside the cavity, see figure 6. The level of fluctuations is largest in the streamwise component, the cross-stream and span-wise being about 61 % and 88 % of the streamwise fluctuations. The adjoint of the critical mode is displayed in figures 6(d-e-f): its spatial structure closely resemble that of the direct mode, with a strong localization along the circular streamlines inside the cavity. As noted above, the direct mode presents a second region of noticeable amplitude near the downstream tip of the cavity and in the shear region just downstream of it, whereas the amplitude of the adjoint mode is not negligible near the upstream tip.

The structural sensitivity of this mode is displayed in figure 7. This quantity indicates the regions in the flow where a feedback forcing proportional to the local perturbation velocity mostly alters the eigenvalue, in other words the wavemaker of the instability. The sensitivity, product of the direct and adjoint mode, is largest inside the cavity, with no significant contributions from the regions of strong shear above it. It is interesting to note that the wavemaker is similar to that computed for a lid-driven square cavity (Haque *et al.* 2012).

To further understand the mechanism related to the first instability appearing in our configuration, we display in figure 8 the 9 components of the sensitivity tensor, see eq. (2.16), in the region inside the cavity. The component S_{ij} denotes the sensitivity to a forcing in the i-direction proportional to the j-component of the instability mode. The results show that the diagonal component are the largest, with forcing clearly located along the streamlines where both the velocity disturbance and its receptivity (given by

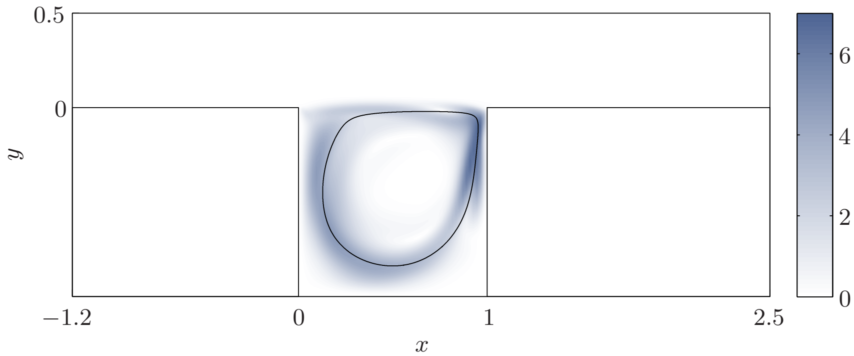

FIGURE 7. Structural sensitivity, the core of the instability, at the neutral conditions, $Re = 1370$, $k = 13.4$, for the flow over an open square cavity. The streamline where the asymptotic analysis predicts the maximum inviscid growth rate is also depicted (see Sec. 7.2).

the adjoint mode) are largest. Noteworthy are also the $\hat{v}^+\hat{u}$ and $\hat{w}^+\hat{u}$ components that reach large amplitudes along the downstream vertical wall limiting the cavity and close to the downstream tip. This reveals a sensitivity to streamwise and spanwise forcing in this region.

5. Instabilities in cavity flows

5.1. *Open cavity & Lid-driven cavity*

The sensitivity analysis performed in the previous section clearly shows that the core of the three-dimensional instability leading to the first bifurcation in a square open cavity is highly localized in space and all contained inside the cavity. This is in contrast with the first 2D instability (Sipp & Lebedev 2007), arising at $Re = 4140$, that is more similar to a wake-type instability (Yamouni *et al.* 2013; Sipp 2012) and localized downstream near the second tip of the cavity.

Examining the results obtained from the stability analysis, it is clear that the external flow plays little role on the generation mechanism of the three-dimensional instability. It is thus reasonable to assume that the configuration studied here is subject to the same type of instabilities as those appearing in a lid-driven cavity (LDC) and discussed by Albensoeder *et al.* (2001) and Albensoeder & Kuhlmann (2006) among others. In the open cavity the shear layer detaching from the upstream corner has the same role as that of the lid in the formation of the vortical motion inside the LDC configuration. The velocity of the lid is uniform while in the present study the fluid velocity along the line connecting the two upper corners is not constant: the velocity starts from zero at the left corner, increases, reaches a maximum and then decreases again vanishing on the downstream corner. In addition, the vertical velocity is different from zero, its magnitude being however smaller than that of the horizontal component. As a result the flow field, although qualitatively similar, also has important differences with respect to that occurring in the lid-driven problem.

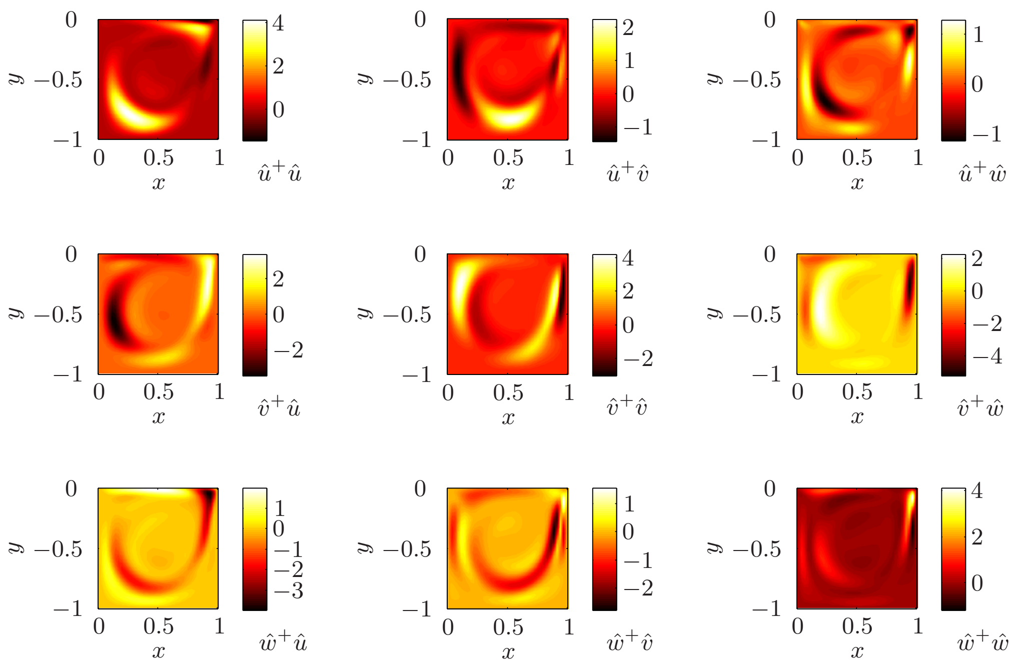

FIGURE 8. Contour plots of the absolute value of structural sensitivity components for the first instability mode at $Re = 1370$, $k = 13.4$, $(L/D = 1)$.

For the closed cavity the critical Reynolds number for the first bifurcation has been calculated independently by Theofilis (2000) and Albensoeder *et al.* (2001) (see also Ding & Kawahara 1998; Shatrov *et al.* 2003). The numerical three-dimensional linear stability analysis of Albensoeder *et al.* (2001) covers a wide range of cavity aspect ratios and present the corresponding unstable modes, which appear to be qualitatively different when varying the cavity aspect ratio. These authors explain the centrifugal instability mechanism in terms of the perturbation energy budget and the criterion proposed by Sipp & Jacquin (2000).

Interestingly, if introducing a (base flow) Reynolds number Re_{av} based on the cavity depth D and on the average velocity $\tilde{U}$ along the line connecting the two opposed corners, the critical Reynolds number for the first instability of the open cavity flow becomes

$$Re_{av} = \frac{\tilde{U}D}{\nu} \approx 490, \tag{5.1}$$

which is around 38% lower than the value found by Albensoeder *et al.* (2001). Despite this difference in the value of the critical Reynolds number, the spanwise wavenumbers at which the instability first occurs are comparable, being $k_{lid} \approx 15.4$ in the LDC case and $k \approx 13.4$ in the present configuration. These qualitative similarities, both in terms of base flows and modes, suggest that the same kind of instability is acting in the two configurations.

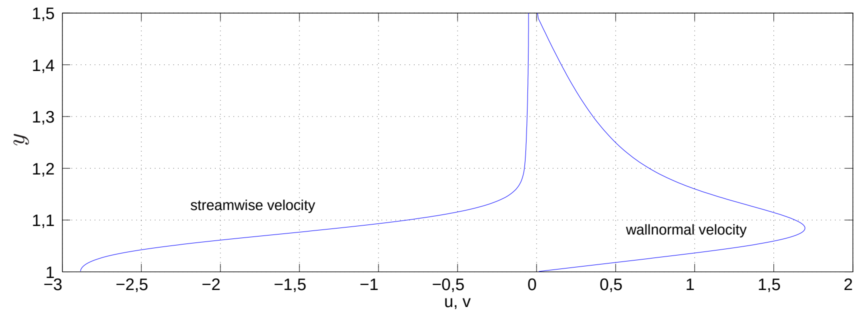

FIGURE 9. Sensitivity of the first bifurcation to streamwise and wall-normal mean velocity modifications at the inflow. The profile shown would provide the largest possible stabilization of the first bifurcation.

5.2. *Link between open cavity flows*

Brés & Colonius (2008) performed direct numerical simulations of open cavity flows for several Re_{δ^*} to investigate the effect of this parameter on the instability properties. In the present configuration the shear layer starts developing at $x^{bl} = -0.4$ (we recall that the origin of our frame of reference is located on the left edge of the cavity) leading to a displacement thickness at the upstream edge ($Re = 1370$)

$$\delta^*(x^{bl}) = \int_0^{0.5} \frac{u_b(x^{bl}, 0.5) - u_b(x^{bl}, y)}{u_b(x^{bl}, 0.5)} dy \approx 0.029. \tag{5.2}$$

Thus, the critical Reynolds number based on this boundary layer thickness is equal to $Re_{\delta^*} = U_\infty \delta^*(x^{bl})/\nu \approx 39.7$.

Here, we wish to show that the starting position of the upstream laminar boundary layer does not affect the critical conditions for the instability when the relevant flow parameter are correctly selected. The main idea is that the dynamics inside the cavity is approximately driven by the average velocity between the two edges rather than by the shear layer thickness, thus strengthening the connection to the lid-driven cavity flow. In order to corroborate this observation, we analyze the critical conditions arising when the incoming free-stream velocity U_∞ is simply linear, i.e. when a Couette profile of velocity $U_\infty(y) = y \cdot \mathbf{e_y}$ is imposed at the inlet.

We observe that there is no reason for the two cases to have the same behavior from a linear stability point of view. However, the first bifurcation in Couette flow (still steady three-dimensional and with a similar spatial structure of that depicted in figure 6) occurs at $Re^{Couette} \approx 20200$ for modes of spanwise wave number $k \approx 13.0$. More interestingly the corresponding Reynolds number $Re_{av} \approx 470$ is in a very good agreement with the value obtained previously (5.1) although the boundary layer thickness of Couette flow is infinity. In light of this result we believe that the averaged Reynolds number Re_{av} is a relevant parameter to predict the onset of instability for open-cavity flows.

6. Structural sensitivity to a velocity based linear feedback

The so-called *sensitivity to base flow variations* is a concept introduced by Bottaro *et al.* (2003), and Marquet *et al.* (2008) within the global framework. In this analysis a small structural velocity-based perturbation acts at the base flow level: the effect of the base flow modifications on the leading eigenvalue of the stability problem allows us to study the different mechanisms that can suppress or enhance the instability. The spatial structure of the so-called adjoint base flow can be used to identify the features of the base flow that provide the main contribution to the instability dynamics and the regions where to locate effective passive control devices. In other words, this modification of the *structure* of the Navier-Stokes operator causes a variation of the base flow which in turn produces a drift of the leading eigenvalue $\gamma = \eta + \mathbf{i}\omega$.

For the sake of brevity, only the main ingredients are outlined here, an extensive and detailed derivation can be found in Marquet *et al.* (2008) and Pralits *et al.* (2010). Using a formalism based on control theory, the eigenproblem (2.6) represents the state equation, the state vector is composed by the global mode $\hat{\mathbf{q}}$ and the complex eigenvalue γ and, the base flow $\boldsymbol{Q_b}$ is the control variable. As in Pralits *et al.* (2010) we express the eigenvalue drift $\delta\gamma$ as

$$\delta\gamma = \delta\eta + \mathbf{i}\delta\omega = \frac{\int_{\mathscr{D}} (\hat{\boldsymbol{u}}\boldsymbol{\cdot}\boldsymbol{\nabla}\hat{\boldsymbol{f}}^{+} - \boldsymbol{\nabla}\hat{\boldsymbol{u}}\boldsymbol{\cdot}\hat{\boldsymbol{f}}^{+})\boldsymbol{\cdot}\delta\,\boldsymbol{u}_b\,dS}{\int_{\mathscr{D}} \hat{\boldsymbol{f}}^{+}\boldsymbol{\cdot}\hat{\boldsymbol{u}}\,dS} \tag{6.1}$$

where $\delta\mathbf{u_b}$ is a generic modification of the base flow. The relation (6.1) provides the effect of a specified velocity distribution implying a dedicated computation for each specific actuation, e.g. wall blowing/suction. The *optimal* boundary velocity distribution, instead, can be directly found as follows (see Meliga & Chomaz 2011)

$$\delta\gamma = \frac{\int_{\partial\mathscr{D}_{w,i,fs}} \left[\left(m_b^{+}\boldsymbol{n} + \frac{1}{Re}\boldsymbol{n}^T\boldsymbol{\cdot}\boldsymbol{\nabla}\boldsymbol{f_b}^{+}\right)\boldsymbol{\cdot}\delta\,\boldsymbol{U}_{w,i,fs}\right] dl}{\int_{\mathscr{D}} \hat{\boldsymbol{f}}^{+}\boldsymbol{\cdot}\hat{\boldsymbol{u}}\,dS} \tag{6.2}$$

where m_b^{+} and $\hat{\boldsymbol{f}}_b^{\,+}$ are the adjoint base flow pressure and the three-dimensional adjoint base flow velocity field and the subscripts w, i, fs indicate the boundaries (inlet, wall or free-slip) on which we calculate the integral. The adjoint base flow field $\boldsymbol{Q_b}^{+}$ must satisfy the following set of linear equations (Pralits *et al.* 2010):

$$\boldsymbol{u}_b \cdot \boldsymbol{\nabla}\boldsymbol{f}_b^{+} - \boldsymbol{\nabla}\boldsymbol{u}_b \cdot \boldsymbol{f}_b^{+} + \frac{1}{Re}\boldsymbol{\nabla}^2\boldsymbol{f}_b^{+} + \boldsymbol{\nabla}m_b^{+} = \hat{\boldsymbol{u}}\boldsymbol{\cdot}\boldsymbol{\nabla}\hat{\boldsymbol{f}}^{+} - \boldsymbol{\nabla}\hat{\boldsymbol{u}}\boldsymbol{\cdot}\hat{\boldsymbol{f}}^{+} \tag{6.3}$$

$$\boldsymbol{\nabla} \cdot \boldsymbol{f}_b^{+} = 0. \tag{6.4}$$

along with the adjoint base flow outlet condition $m_b^{+}\mathbf{n} - Re^{-1}\mathbf{n}\cdot\nabla\boldsymbol{f_b}^{+} = -(\boldsymbol{u_b}\cdot\mathbf{n})\boldsymbol{f_b}^{+} + (\hat{\boldsymbol{u}}\cdot\mathbf{n})\hat{\boldsymbol{u}}^{+}$ at $\partial\mathscr{D}_{out}$ and zero-velocity conditions at the solid walls and at the inlet.

The sensitivity of the instability with respect to the incoming flow is examined first. Figure 9 shows both the sensitivity to the stream-wise and the wall-normal components of the inflow velocity profile, where the profiles shown would provide the optimal decrease of the instability growth rate. The x-component is found to be always negative and attains significant values only near the wall. This fact is not surprising because the base flow modifications have effect only if related to the shear layer that drives the core vortex inside the cavity. Perturbations in the free stream do not affect the flow at the edge and inside the cavity, the regions where the instability is triggered. Negative modifications of the inlet velocity profile cause stabilization due to decrease of the momentum inside the shear layer. The effect of the wall-normal component is related to the same mechanism, decreasing of the total streamwise momentum at the cavity tip by normal advection.

In view of an active control of the first bifurcation, we depict the wall-normal component of the sensitivity along the cavity walls in figure 10; this corresponds to the optimal blowing/suction profiles giving the largest stabilization. We see that the sensitivity is vanishing along the first free-slip boundary just downstream of the inflow ($y = 0; -1.2 < x < -0.4$), while a combination of blowing and suction is found to

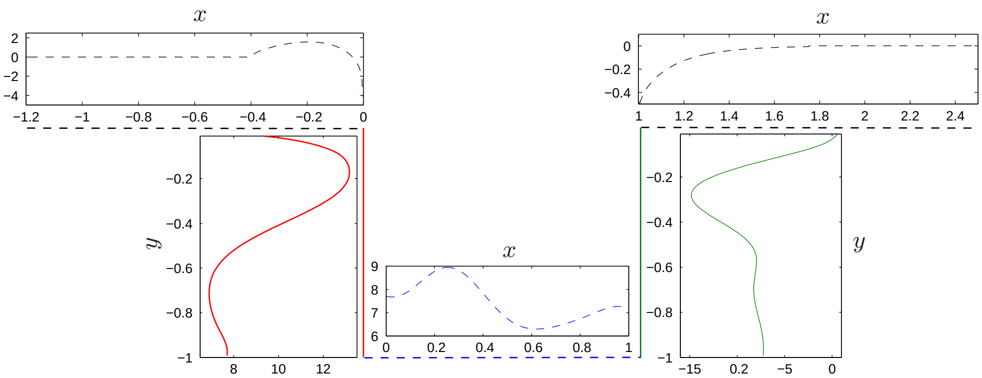

FIGURE 10. Sensitivity to boundary conditions on the five walls defining the open cavity flow. Wall-normal blowing and suction is applied on each wall with positive velocity indicating blowing and assuming stabilization, i.e. the profiles shown on each wall would provide the optimal decrease of the instability growth rate.

be optimal on the wall upstream of the cavity ($y = 0; -0.4 < x < 0$). Inside the cavity, on both lateral walls, a stabilizing normal component is directed in the streamwise direction. The optimal blowing and suction on the lower wall would create a flow opposite to the vortex inside the cavity, thus trying to quench it. The analysis, finally, shows that it is not possible to significantly modify the instability by applying control on the downstream wall (lowest sensitivity magnitude).

7. Asymptotic inviscid stability theory

The spatial distribution of the structural sensitivity (that is spatially concentrated around a streamline inside the cavity) suggests the possibility to use the *local theory* to describe the evolution of the instability and provide a more quantitative evidence for the mechanism from which it arises. An appealing approach in this context is offered by the short-wavelength approximation (WKBJ) developed by Bayly (1988).

This approach is shortly outlined here, for a more detailed presentation the reader is referred to Lifschitz & Hameiri (1991); Lifschitz (1994) and references therein. The solution of the linearised Navier–Stokes equations is sought in the form of a rapidly oscillating and localised wave-packet evolving along the *Lagrangian trajectory* $\mathbf{X}(t)$ and characterised by a *wave-vector* $\mathbf{k}(t) = \nabla\phi(\mathbf{X}, t)$ and an *envelope* $\mathbf{a}(\mathbf{X}, t)$ such that

$$\mathbf{u}(\mathbf{X}, t) = \mathrm{e}^{\mathrm{i}\phi(\mathbf{X},t)/\epsilon}\mathbf{a}(\mathbf{X}, t, \epsilon) = \mathrm{e}^{\mathrm{i}\phi(\mathbf{X},t)/\epsilon}\sum_n \mathbf{a}_n(\mathbf{X}, t)\epsilon^n \tag{7.1}$$

$$p(\mathbf{X}, t) = \mathrm{e}^{\mathrm{i}\phi(\mathbf{X},t)/\epsilon}b(\mathbf{X}, t, \epsilon) = \mathrm{e}^{\mathrm{i}\phi(\mathbf{X},t)/\epsilon}\sum_n b_n(\mathbf{X}, t)\epsilon^{n+1} \tag{7.2}$$

where $\epsilon \ll 1$ and $\mathbf{X} = \epsilon\mathbf{x}$ is a slowly varying variable. In the limit of vanishing viscosity ($Re \to \infty$) and large wavenumbers ($||\mathbf{k}|| \to \infty$), the theory provides the leading order term for the growth rate associated with a localised perturbation. This is obtained by integrating the following set of ordinary differential equations

$$\frac{D\mathbf{k}}{Dt} = -\mathcal{L}^t(\mathbf{X})\mathbf{k}, \tag{7.3}$$

$$\frac{D\mathbf{a}}{Dt} = \left(\frac{2\mathbf{k}\mathbf{k}^T}{|\mathbf{k}|^2} - \mathcal{I}\right)\mathcal{L}(\mathbf{X})\mathbf{a}, \tag{7.4}$$

along the Lagrangian trajectories defined by the ODE

$$\frac{D\mathbf{X}(t)}{Dt} = \mathbf{u}_b(X(t), t)\ . \tag{7.5}$$

In the equations above $\mathcal{L} = \nabla\mathbf{u}_b$ is the base-flow velocity gradient tensor and $\mathcal{I}$ the identity matrix. Since the flow under investigation is steady, the Lagrangian trajectory corresponds to the streamlines of the base flow. Three initial conditions have to be assigned to solve the problem above: $\mathbf{k}(t=0) = \mathbf{k}_0$, $\mathbf{a}(t=0) = \mathbf{a}_0$ and $\mathbf{x}(t=0) = \mathbf{x}_0$. The last condition imposes the Lagrangian origin of the streamline and thereby entirely identifies it.

Lifschitz & Hameiri (1991) proved that a sufficient condition for inviscid instability is that the system of eqs. (7.3), (7.4) and (7.5) has at least one solution for which $\|\mathbf{a}(t)\| \to \infty$ as $t \to \infty$. This theory has been successfully applied in the past to study elliptic, hyperbolic and centrifugal instabilities of two-dimensional stationary base flows (Sipp *et al.* 1999; Godeferd *et al.* 2001). In order to characterize the instability mechanism arising inside the cavity with such local theory, the self-excited nature of the instability must be properly accounted for. In this context, a central role is played by closed Lagrangian trajectories (closed streamlines in our case), i.e. orbits described by material points which return to their initial positions after a given time T (the period of revolution of a material particle). These closed trajectories play a special role in the dynamics of the instability: on the closed orbits, local instability waves propagate and feedback on themselves leading to a self-excited unstable mode.

To apply the theory, both equations (7.3) and (7.4) must be integrated along the closed orbits existing inside the cavity. Since the base flow is steady and the streamlines are closed, eq. (7.3) is a linear ODE with periodic coefficients whose general solution can be written in terms of Floquet modes. In particular, the solution can be found by building the fundamental Floquet matrix $\mathcal{M}(T)$, solution of the system

$$\frac{D\mathcal{M}}{Dt} = -\mathcal{L}^t(\mathbf{X})\mathcal{M} \quad \text{with} \quad \mathcal{M}(0) = \mathcal{I}\ , \tag{7.6}$$

and extracting its eigenvalues and the corresponding eigenvectors. Using these eigenvectors as initial conditions, it is possible to retrieve the temporal evolution of $\mathbf{k}$ during a lap around the closed streamline. Equation (7.3) admits three independent solutions related to the 3 eigenvectors of the fundamental Floquet matrix $\mathcal{M}(T)$. However, since the base flow is two-dimensional, there exists for each orbit one eigenvalue equal to 1 with the corresponding eigenvector that remains constant in time and orthogonal to the base flow. In other words, since the third column of $\mathcal{L}$ and the third line of $\mathcal{L}^t$ are zero, the transverse component of $\mathbf{k}$ remains constant as time evolves. In contrast, the in-plane components evolve under the action of the deformation tensor. Once equation (7.3) is solved, the amplitude $\mathbf{a}$ can be found by integrating equation (7.4). One can use any linear combination of the Floquet modes from equation (7.6) to set the specific $\mathbf{k}$ in equation (7.4).

Since we are trying to determine a self-excited mode, we need only to consider solutions of (7.3) that are periodic in time, i.e. solutions such that $\mathbf{k}(0) = \mathbf{k}(T)$. Moreover Bayly (1988), Sipp & Jacquin (2000) and Lifschitz & Hameiri (1991) have shown that centrifugal and hyperbolic instabilities do attain their maximum growth rate for modes characterized by purely transverse wavenumbers. Therefore, only eigenvectors orthogonal

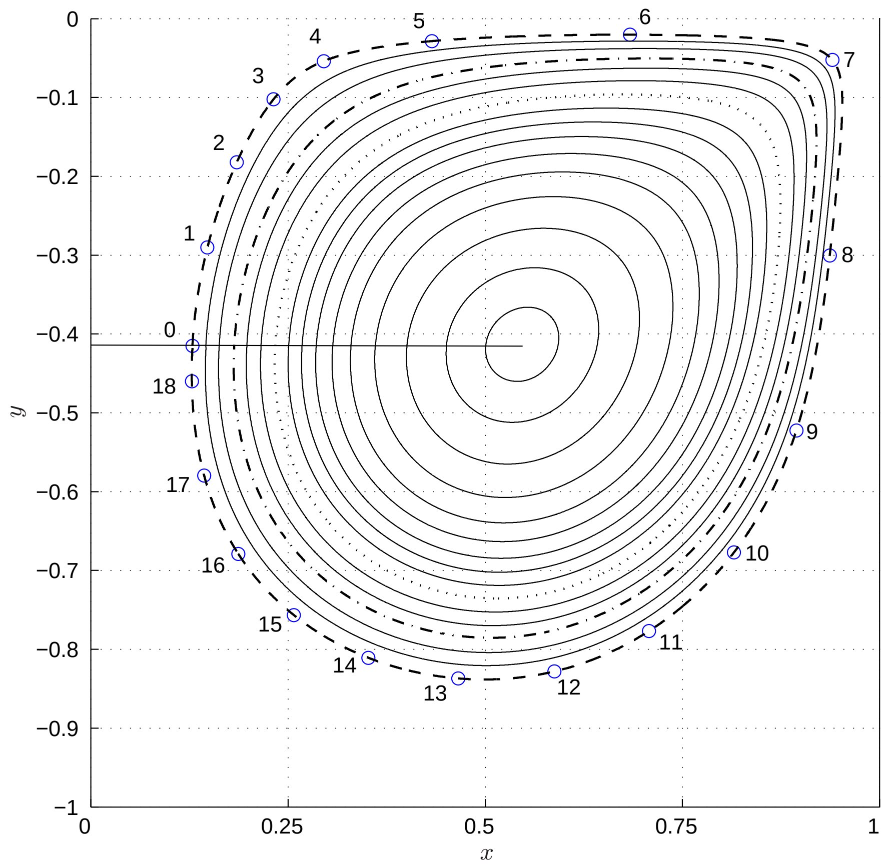

FIGURE 11. Streamlines for the flow inside the cavity at $Re = 1370$. The asymptotic inviscid stability theory identifies three streamlines along which three different WKBJ modes present their maximum growth rate: $(-\ -)$ orbit of the global maximum growth rate pertaining to the steady mode σ_∞ (see fig. 12); $(-\cdot-)$ orbit of the unsteady mode related to σ_2 ; $(\cdot\cdot\cdot)$ orbit of the steady mode related to σ_3. The evolution of a particle along the streamline $(-\ -)$ is also depicted. The revolution period of this streamline is $T = 18.3$. The horizontal line connecting the centre of the vortex to the left wall of the cavity is used in the present work to parametrize the streamlines.

to the base flow will be considered in the following analysis. Solutions of eq. (7.4) associated with a $\mathbf{k}$ orthogonal to the plane of motion are usually termed *pressureless modes* (see also Godeferd *et al.* 2001). With this choice, eq. (7.4) reduces to an ordinary linear differential equation with periodic coefficients. According to Floquet theory, its solution can be written in terms of Floquet modes

$$\mathbf{a}(t) = \bar{\mathbf{a}}(t)\ \exp(\sigma t)\ , \tag{7.7}$$

where $\bar{\mathbf{a}}(t)$ is a periodic function (same period T as the material point moving along the selected closed streamline) and $\Re\{\sigma\} = \sigma_r$ is the growth rate of the perturbation. In order to make a quantitative comparison with the eigenvalues predicted by the global analysis, we have to compute the values of σ in (7.7) for each closed orbit inside the

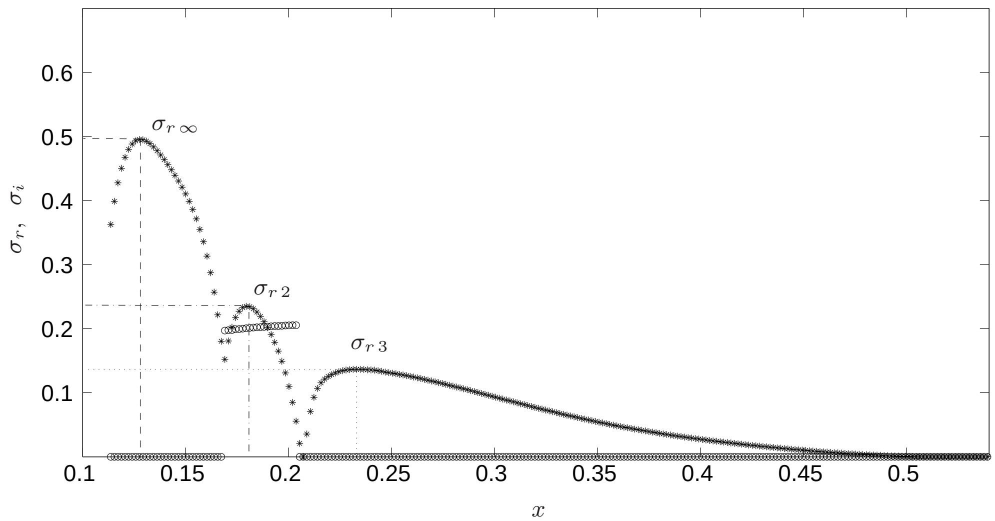

FIGURE 12. WKBJ growth rate σ_r $(*)$ and eigen-frequency σ_i $(\circ)$ at $Re_{\mathcal{BF}} = 1370$. Here the parameter x is the physical coordinate showed in fig. 11. The lines denote the maximum of the different branches: $(-\ -)$ maximum inviscid growth rate $\sigma_{r\,\infty}$; $(-\ \cdot\ -)$ maximum related to second branch $\sigma_{r\,2}$; $(\cdot\ \cdot\ \cdot)$ third maximum $\sigma_{r\,3}$.

cavity. To this end, we parametrize each streamline, and the corresponding growth rate σ, with the distance along the horizontal line connecting the centre of the vortex to the left wall of the cavity (see fig. 11).

As for eq. (7.3), the fundamental Floquet matrix $\mathcal{A}$ corresponding to equation (7.4) is built by integrating the system

$$\frac{D\mathcal{A}}{Dt} = \left(\frac{2\mathbf{k}\mathbf{k}^T}{|\mathbf{k}|^2} - \mathcal{I}\right)\mathcal{L}(\mathbf{X})\mathcal{A}, \tag{7.8}$$

$$\mathcal{A}(0) = \mathcal{I}; \tag{7.9}$$

along each orbit. The eigenvalues $\mu_i(x_0)$ and the corresponding eigenvectors of $\mathcal{A}(T)$ are then easily extracted.

As mentioned above, since the base flow is two-dimensional and the wavevector $\mathbf{k}$ is orthogonal to the $x-y$ plane, we expect one eigenvalue of $\mathcal{A}$ to be 1. The other two, for the incompressibility constrain, must multiply to 1, i.e. $\mu_1(x_0)\ \mu_2(x_0) = 1$. The Floquet exponent $\sigma(x_0)$ of the perturbation on the selected orbit ψ_0 is obtained from the Floquet multiplier $\mu(x_0)$ of $\mathcal{A}$ by the simple relation

$$\sigma^{\{n\}}(\psi_0) = \sigma_r(\psi_0) + i\sigma_i^{\{n\}}(\psi_0) = \frac{\log(\mu)}{T(\psi_0)} + \mathrm{i}\frac{2n\pi}{T(\psi_0)} \ \text{ with } n \in \mathbb{N} \tag{7.10}$$

where $T(\psi_0)$ is the period of revolution.

The growth rate of each WKBJ mode is simply given by the real part of $\sigma^{\{n\}}$. The frequency is related to the imaginary part and is not unique. According to the formula (7.10), modes with the same growth rate (at leading order) but different frequencies are admissible: in particular the admissible frequencies are integer multiple of the frequency of revolution along the same streamline.

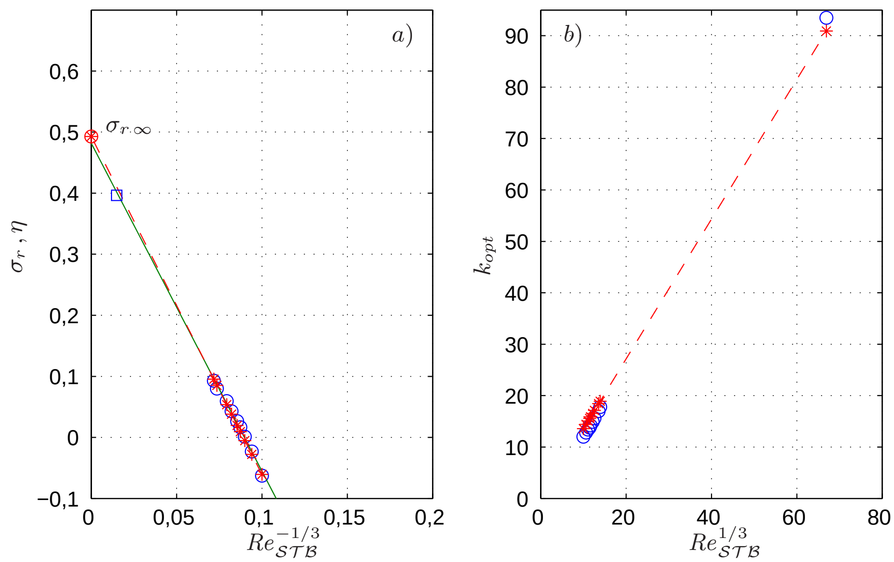

FIGURE 13. (Colour online) Global and Asymptotic stability results. a) Viscous growth rate η ((◯) and (□) = $Re_{\mathcal{STB}} = 300000$) at $Re_{\mathcal{BF}} = 1370$ and asymptotic estimate of growth rate σ_r ($*$ $--$) according to the correction in Appendix A. We depict also the regression line ($-$) related to the global growth rates. b) Optimal global spanwise wavenumber k_{opt} (◯) and prediction from the asymptotic theory ($*$) as a function of $Re_{\mathcal{STB}}^{1/3}$. The predicted optimal spanwise wavenumber is simply obtained by finding the maximum of the scaling law (A 4), i.e. $k = (Re_{\mathcal{STB}}A/2)^{1/3}$.

7.1. *Asymptotic estimate of the first bifurcation*

The numerical computations of the asymptotic stability are performed on the same base-flow fields used for the global stability analysis. Several numerical methods are available to solve the system of ODEs (7.5-7.8) along with their initial conditions. We chose a $4-th$ order Runge-Kutta method: starting from the points located on the horizontal line, connecting the centre of the vortex to the left wall of the cavity (see Figure 11), the algorithm marches along the orbits ensuring the spatial periodicity of each streamline. In the figure we also report the position of a material point along its trajectory at equal time intervals to give a visual impression of the local velocity along the streamline.

The asymptotic eigenpairs have been computed with several discretizations and only the eigenvalues with an accuracy of four significant digits are presented. In figure 12, we show the real and imaginary part of the eigenvalues obtained with the WKBJ approximation as function of the x coordinate defining the different orbits.

The asymptotic analysis reveals three maxima of the growth rates $\sigma_{r\,\infty}(=\sigma_{r\,1})$, which is also the global maximum, $\sigma_{r\,2}$ and $\sigma_{r\,3}$. The first and the third branch (σ_1 & σ_3) are characterized by zero frequency eigenvalues, while the second branch (σ_2) is associated to unstable oscillations with frequency of ≈ 0.2. As further discussed below, the closed streamline of maximum growth rate $\sigma_{r\,\infty}$ is located within the wavemaker of stationary unstable global mode.

However, despite this agreement, the viscous correction term and the correction term relative to finite wavenumber effects need to be taken into account for a correct prediction of the instability, see Landman & Saffman (1987); Gallaire *et al.* (2007).

In figure 13a) we report the growth rate of the unstable mode computed on the base

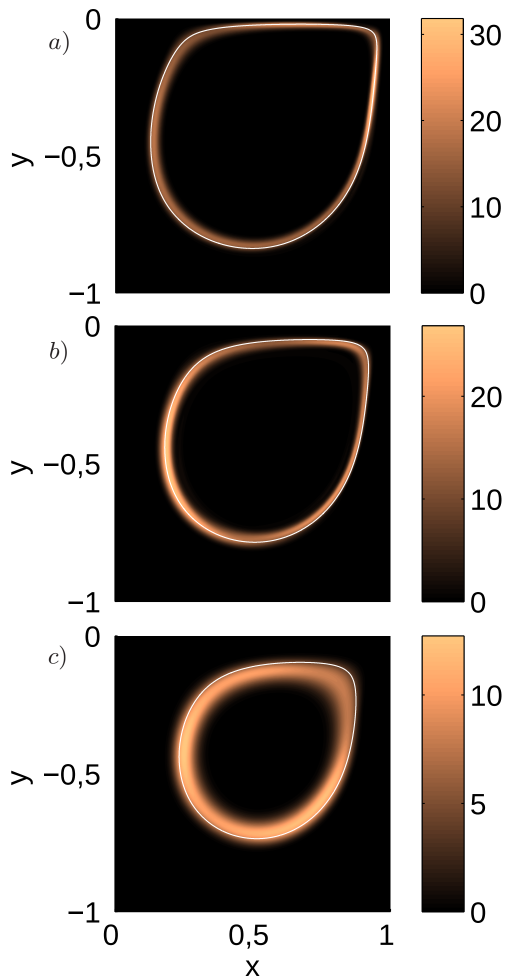

FIGURE 14. Comparison between the optimal streamline of WKBJ branches and Sensitivity Maps related to (global) eigenvalues: a) $0.36 + i0.00$; b) $0.14 + i0.20$; c) $0.07 + i0.00$. Parameter settings: $Re_{\mathcal{BF}} = 1370$, $Re_{\mathcal{STB}} = 300000$ & $k = 93.5$.

flow at $Re_{\mathcal{BF}} = 1370$ when increasing the Reynolds number in the linearized stability equations, $Re_{\mathcal{STB}}$, and the growth rate obtained by integrating along the closed orbits with the corrections discussed in Appendix A,

$$s = \sigma(\psi_0) - \frac{A}{k} - \frac{k^2}{Re_{\mathcal{BF}}}. \tag{7.11}$$

The value of A above is not estimated by a least square fitting as in previous studies, but computed analytically using the informations provided by the local adjoint and direct field on the streamline. The values obtained with this procedure are reported in Table 2. Figure13a) shows that the scaling provided by the global stability analysis estimates correctly the asymptotic growth rate $\sigma_{r\,\infty}$. The corresponding optimal spanwise wavenumber k is also depicted in 13b) as a function of $Re_{\mathcal{STB}}^{1/3}$. The spanwise wavenumber, as maximal growth rate, follows the correct scaling laws, $\sigma_r \propto Re_{\mathcal{STB}}^{-1/3}$ and $k_{opt} \propto Re_{\mathcal{STB}}^{1/3}$ (Bayly 1988; Sipp *et al.* 1999).

Δt_{orbit}	k	$\mathscr{J}$	A
0.005	13.4	0.00637	5.1143
0.0025	13.4	0.00678	5.0148
0.001	13.4	0.00681	5.0078

TABLE 2. Convergence of parameters arising in the asymptotic estimation (see Appendix A) of the viscous growth rate. Δt_{orbit} is the step used to discretize the critical orbit. (Here, $Re_{\mathcal{BF}} = 1370$)

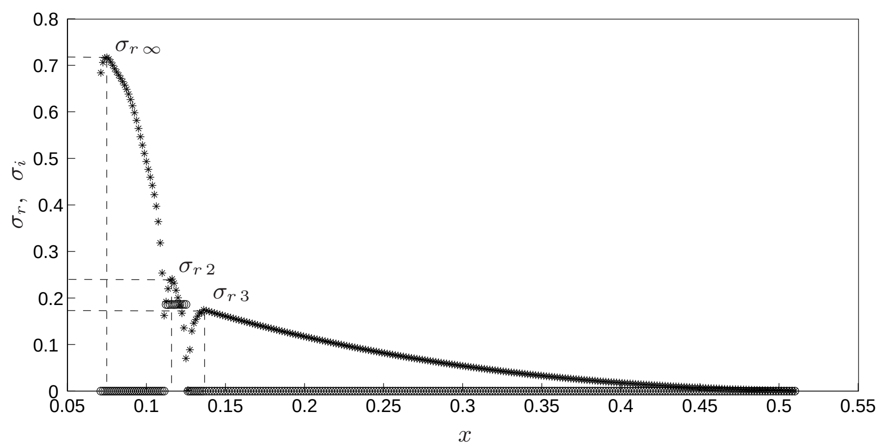

FIGURE 15. Asymptotic results for $Re_{\mathcal{BF}} = 4140$. See Figure 12 for details.

Finally, we focus our attention on the spatial distribution of the structural sensitivity fields computed with the maximum $Re_{\mathcal{STB}}$ considered (equal to 300000). Figure 14a) shows the agreement between the critical streamline (i.e. the streamline ψ where the inviscid growth rate is maximum) and the sensitivity map. At large (stability) Reynolds numbers $Re_{\mathcal{STB}}$, therefore, the sensitivity analysis indicates that the instability core is located on the orbit with maximum growth rate.

The global analysis performed at $Re_{\mathcal{BF}}$ provides also informations about the sub-critical branches arising in the asymptotic computations. We depict the structural sensitivity extracted from the global analysis of these two sub-critical WKBJ eigenmodes in Figure 14b) and 14c). As for the leading eigemode we observe an excellent correspondence between the sensitivity spatial map and the two critical orbits. Interestingly, we note also the agreement between the frequency of mode σ_2 (see figure 14b) and the frequency predicted by the WKBJ analysis. From a physical point of view, this matching can be associated to the fact that these eigenmodes are of centrifugal nature, i.e. inviscid, and therefore the *inviscid* structural sensitivity is able to isolate accurately the regions where each of the three instability branches presents the main contribution to the instability mechanism.

7.2. *Asymptotic results for $Re_{\mathcal{BF}} = 4140$*

As previously discussed, when we consider the stability to three dimensional perturbations at supercritical Reynolds numbers, we find several unstable branches (see figure 3). If we consider the spanwise wavenumber $k = 22$ and $Re_{\mathcal{BF}} = 4140$, we observe the occurrence of several harmonics of the fundamental leading eigenvalue. As shown in fig-

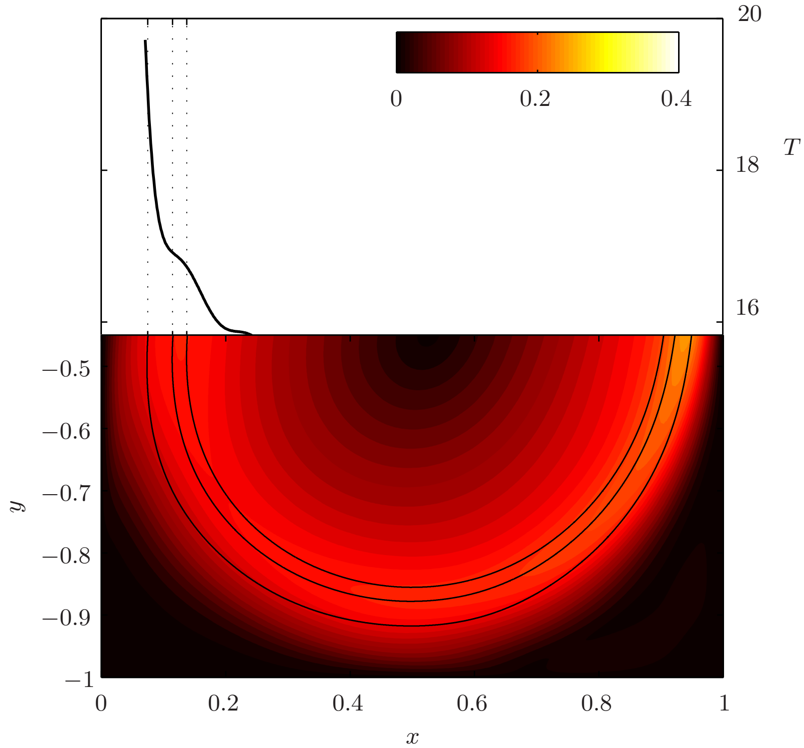

FIGURE 16. Up) Revolution period of cavity orbits as a function of the abscissa x. Down) Contour plot of the base flow modulus ($||\boldsymbol{u}_b||_2$) at $Re_{\mathcal{BF}} = 4140$ and the three streamlines corresponding to the local maxima of the inviscid growth rate in figure 15.

ure 3b), these modes are characterized by a quantized eigenfrequency, $\omega \approx 0.32n$ with n integer. To show that the asymptotic analysis is able to accurately predict also the frequency of these harmonics, we carry out computations for the base flow at Reynolds number $Re_{\mathcal{BF}} = 4140$ and report the results in figure 15, using the same conventions used for the onset of the bifurcation, $Re_{\mathcal{BF}} = 1370$ in figure 12. We first need to identify the closed streamlines and then calculate the instability properties along the orbit. We observe again three local maxima of the asymptotic growth rate, corresponding to two steady and one time-depedent modes.

The variation of the revolution period T as a function of the coordinate x, defining the different orbits, is depicted in the top panel of figure 16, while the corresponding orbits inside the cavity are displayed in the lower panel. The main result we present here is that the period of the higher harmonics of the zero-frequency leading mode is selected by the period of revolution along the streamline of maximum growth rate. In table 3 we show that indeed the frequencies obtained from the global stability analysis and displayed in figure 3 corresponds to the frequency computed by the local analysis (eq. 7.10). It is interesting to note that the global mode frequencies are uniquely related to the revolution period of a Lagrangian particle transported along the orbit. Thus, we conclude that the different frequencies of the multiple unstable branches are obtained as

Harmonic	Global mode frequency	Orbit Period	WKBJ frequency	Percentual Error
n	ω	T	$\sigma_i^{\{n\}}(\psi_0) = 2n\pi/T$	
0	0.000	19.5	0.00	–
1	0.302	19.5	0.32	4.2%
2	0.610	19.5	0.64	4.7%
3	0.920	19.5	0.96	4.5%

TABLE 3. Comparison of the results obtained using Global stability analysis with those provided by the Asymptotic analysis. We selected the orbit that has the maximum inviscid growth rate using a base flow characterized by $Re_{\mathcal{BF}} = 4140$. The WKBJ frequencies are calculated according to (7.10).

multiple n of the period of revolution along the critical (most unstable) orbit; the data in the table show an error lower than the 5%.

8. Final remarks

In this work, we study the instability of the flow past an infinitely wide open square cavity. First, we identify the critical Reynolds number ($Re_{\mathcal{BF}} = 1370$) at which the first bifurcation occurs. This instability drives the flow from a steady two-dimensional to a steady three-dimensional configuration characterized by a relatively short modulation in the spanwise direction, the spanwise scale of the modulation being of about 0.47 cavity depths.

The spatial structure of the direct and adjoint eigenmodes are examined to describe the features of the flow past the pitchfork bifurcation. The direct mode field is concentrated inside the cavity in a circular region with a tail on the shear region just above the downstream wall; the adjoint mode has a similar structure except for the small region near the upstream edge of the cavity where the flow is most receptive to momentum forcing. The overlapping of these two fields provides information about the instability mechanism (the so-called wavemaker) and is concentrated within the square cavity suggesting that the generation of the instability mechanism is spatially concentrated around a closed streamline inside the cavity, around the core vortex.

We examine different types of cavity flows (i.e. characterized by different boundary conditions) to identify a correct scaling for the critical Reynolds number at which the first bifurcation occurs. Indeed, for both open and lid-driven cavity, the flow first becomes unstable to three-dimensional steady perturbation. Interestingly we observe that the mean velocity computed along the line connecting the two opposed edge, allows us to roughly estimate the critical conditions at which the first bifurcation arises. The critical value of a Reynolds number based on this averaged velocity, the cavity depth and the fluid viscosity is found to be $Re_{av} \approx 470$ for the different configurations studied in literature. In addition, we show that the thickness of the boundary layer at the upstream edge of the cavity has a weak influence on the instability onset.

The sensitivity to base-flow modifications is then considered to study the mechanisms that can suppress or enhance the instability. We follow here the approach by Meliga & Chomaz (2011) and compute the optimal linear velocity distribution at the walls and at the inlet of the computational domain able to stabilize the flow. The resulting blowing/suction profiles show that each modification (when possible) is aimed to decrease the total momentum of the cavity core vortex (identified above as the *core* of the instability).

The WKBJ approximation is then introduced to predict the first instability and its characteristics as suggested by Bayly (1988). Considering the asymptotic stability along the closed streamlines inside the cavity, we find three different branches of unstable orbits (2 stationary branches and an unsteady branch) and select the three critical orbits ψ whose corresponding growth rates are local maxima ($\sigma_{r\,\infty}, \sigma_{r\,2}, \sigma_{r\,3}$). The asymptotic values of the growth rate and of the spanwise wavenumber of the unstable modes show very good agreement with the global stability analysis once the correction for finite Reynolds number and spanwise length scale are applied to the inviscid asymptotic result. The three critical orbits detected by the asymptotic analysis are also shown to overlap with the structural sensitivity map of unstable modes at low viscosities, large $Re_{\mathcal{STB}}$ (we refer to this field as *inviscid* structural sensitivity). This procedure allows us to identify the spatial region where the core of the inviscid mechanism of the instability is located.

To identify a frequency selection mechanism for the time-dependent subleading unstable global modes emerging at supercritical conditions, we consider the stability of the flow at $Re_{\mathcal{BF}} = 4140$ where the global analysis shows the occurrence of 4 branches of unstable modes characterized by frequencies that are multiple of a fundamental value ω_0. We show that the value of ω_0 corresponds to the period of revolution of Lagrangian fluid particles along the closed orbit of largest growth rate in the asymptotic limit. We thus conclude that the asymptotic theory is able to predict accurately the global stability results, enabling us to estimate the critical conditions leading to the instability. Furthermore, the *inviscid* structural sensitivity, discussed here, is a general concept that can be used whenever the instability is of inviscid type.

Appendix A. Construction of pressureless modes

In what follows we briefly recall the theory related to the dynamics of asymptotic modes (Bayly 1988). First of all, we express the evolution of the perturbation using the normal mode ansatz

$$[\boldsymbol{u}', P'] = [\hat{\boldsymbol{u}}, \hat{P}] exp\{ikz + st\}.$$

The main idea is to use the eigenpairs of the fundamental Floquet matrix $\mathcal{M}(T)$ to build a vector basis $\mathbf{f}_i$ for the representation of the modes along the orbit:

$$\hat{\boldsymbol{u}}(\mathbf{x}) = \sum_{i=1}^{3} \hat{u}_i(\mathbf{x})\mathbf{f}_i(\mathbf{x}). \tag{A 1}$$

This basis diagonalize the non-linear operator $\boldsymbol{u}_b \cdot \nabla() + () \cdot \nabla \boldsymbol{u}_b$ and can be computed as $\mathbf{f}_i = e^{-\sigma t}\mathcal{M}(t)\mathbf{e_i}$. Considering the limit of $||\mathbf{k}|| \to \infty$, we re-scale the WKBJ eigenmode as:

$$[\hat{\mathbf{u}}, \hat{\mathbf{v}}, \hat{\mathbf{w}}, \hat{\mathbf{p}}](\tilde{\Psi}) = [\hat{\mathbf{U}}, \hat{\mathbf{V}}/k, \hat{\mathbf{w}}/\sqrt{k}, \hat{\mathbf{p}}/k\sqrt{k}](\tilde{\Psi}) \tag{A 2}$$

where the new streamfunction $\tilde{\Psi} = \sqrt{k}(\psi - \psi_0)$ allows us to magnify the region near the critical orbit ψ_0. Introducing the scaling (A 2) into the linearized Euler equations, we get the equation of a quantum harmonic oscillator (see e.g. Bender & Orszag 1978),

$$\hat{\mathbf{U}}''(\tilde{\Psi}) + \left[\frac{A}{\mathscr{J}(\psi_0)} - \lambda^2\tilde{\Psi}^2\right]\hat{\mathbf{U}} = 0 \tag{A 3}$$

with $\hat{\mathbf{U}}(\pm\infty) = 0$; $\lambda^2 = -\sigma''(\psi_0)/(2\mathscr{J})$ and

$$\mathscr{J} = 1/T(\psi_0)\int_0^{T(\psi_0)} (\mathbf{f}_1^\dagger \cdot \nabla\psi)\left[\sigma(\psi_0) + \frac{d}{dt}\right]\{\mathbf{f}_1 \cdot \nabla\psi\}dt.$$

In eq. (A 3), the constant A is the parameter that governs the scaling of the eigenvalue s (i.e. $s = \sigma(\psi_0) - A/k$) and the adjoint vector $\mathbf{f}_i^\dagger$ is normalized as $\mathbf{f}_i^\dagger \cdot \mathbf{f}_j = \delta_{ij}$.

A better quantitative estimate of the viscous growth rate can be achieved using the viscous correction introduced by Landman & Saffman (1987) (see also Gallaire *et al.* 2007). The composite estimation thus reads:

$$s = \sigma(\psi_0) - \frac{A}{k} - \frac{k^2}{Re_{\mathcal{BF}}}. \qquad \text{(A 4)}$$

REFERENCES

Albensoeder, S. & Kuhlmann, H.C. 2006 Nonlinear three-dimensional flow in the lid-driven square cavity. *J. Fluid Mech.* **569**, 465–480.

Albensoeder, S., Kuhlmann, H. C. & Rath, H. J. 2001 Three-dimensional centrifugal-flow instabilities in the lid-driven-cavity problem. *Phys. Fluids* **13**, 121–136.

Amestoy, P. R., Duff, I. S., Koster, J. & L'Excellent, J.-Y. 2001 A fully asynchronous multifrontal solver using distributed dynamic scheduling. *SIAM Journal on Matrix Analysis and Applications* **23** (1), 15–41.

Amestoy, P. R., Guermouche, A., L'Excellent, J.-Y. & Pralet, S. 2006 Hybrid scheduling for the parallel solution of linear systems. *Parallel Computing* **32** (2), 136–156.

Arnoldi, W. E. 1951 The principle of minimized iteration in the solution of the matrix eigenproblem. *Quart. Appl. Math.* **9**, 17–29.

Barbagallo, A., Sipp, D. & Schmid, P. J. 2009 Closed-loop control of an open cavity flow using reduced-order models. *J. Fluid Mech.* **218**, 1–50.

Bayly, B. J. 1988 Three-dimensional centrifugal-type instabilities in inviscid two-dimensional flows. *Phys. Fluids* **31**, 56–64.

Bayly, B. J. 1989 Computations of broad-band instabilities in a class of closed-streamline flows. In *Mathematical aspects of vortex dynamics; edited by R. E. Caflisch, Philadelphia, PA, Society for Industrial and Applied Mathematics*, pp. 50–58.

Bender, C. M. & Orszag, S. A. 1978 *Advanced Mathematical Methods For Scientists and Engineers*. McGraw-Hill, New-York.

Bottaro, A., Corbett, P. & Luchini, P. 2003 The effect of base flow variation on flow stability. *J. Fluid Mech.* **476**, 293–302.

Brés, G. A. & Colonius, T. 2008 Three-dimensional instabilities in compressible flow over open cavities. *J. Fluid Mech.* **599**, 309–339.

Ding, Y. & Kawahara, M. 1998 Linear stability of incompressible flow using a mixed finite element method. *J. Comput. Phys.* **139**, 243–273.

Gallaire, F., Marquillie, M. & Ehrenstein, U. 2007 Three-dimensional tranverse instabilities in detached boundary layers. *J. Fluid Mech.* **571**, 221–233.

Gharib, M. & Roshko, A. 1987 The effect of flow oscillations on cavity drag. *J. Fluid Mech.* **177**, 501–530.

Giannetti, F. & Luchini, P. 2007 Structural sensitivity of the first instability of the cylinder wake. *J. Fluid Mech.* **581**, 167–197.

Godeferd, F. S., Cambon, C. & Leblanc, S. 2001 Zonal approach to centrifugal, elliptic and hyperbolic instabilities in stuart vortices with external rotation. *J. Fluid Mech.* **449**, 1–37.

Haque, S., Lashgari, I., Giannetti, F. & Brandt, L. 2012 Stability of fluids with shear-dependent viscosity in the lid-driven cavity. *J. Non-Newton. Fluid Mech.* **173-174**, 49–61.

Landman, M. J. & Saffman, P. 1987 The three-dimensional instability of strained vortices in a viscous fluid. *Phys. Fluids* **30**, 2339–2342.

Lehoucq, R., Maschhoff, K., Sorensen, D. & Yang, C. 2007 Arpack software. website: http://www.caam.rice.edu/software/arpack/ .

Lifschitz, A. 1994 On the instability of certain motions of an ideal incompressible fluid. *Adv. Appl. Maths* **15**, 404–436.

Lifschitz, A. & Hameiri, E. 1991 Local stability conditions in fluid dynamics. *Phys. Fluids A* **3**, 2644–2651.

Luchini, P. & Bottaro, A. 2014 Adjoint equations in stability analysis. *Annu. Rev. Fluid Mech.* **46** (1), 493–517.

Marquet, O., Sipp, D. & Jacquin, L. 2008 Sensitivity analysis and passive control of cylinder flow. *J. Fluid Mech.* **615**, 221–252.

Meliga, P. & Chomaz, J. M. 2011 Global modes in a confined impinging jet: application to heat transfer and control. *Theor. Comp. Fluid Dyn.* **25**, 179–193.

Pralits, J.O., Brandt, L. & Giannetti, F. 2010 Instability and sensitivity of the flow around a rotating circular cylinder. *J. Fluid Mech.* **650**, 513–536.

Rockwell, D. & Naudascher, E. 1978 Review – self-sustaining oscillations of flow past cavities. *J. Fluids Eng.* **100**, 152–165.

Rossiter, J. E. 1964 Wind-tunnel experiments on the flow over rectangular cavities at subsonic and transonic speeds. *Tech.Rep.* **3438**.

Rowley, C. W., Colonius, T. & Basu, A. J. 2002 On self-sustained oscillations in two-dimensional compressible flow over rectangular cavities. *J. Fluid Mech.* **455**, 315–346.

Shatrov, V., Mutschke, G. & Gerbeth, G. 2003 Three-dimensional linear stability analysis of lid-driven mhd cavity flow. *Phys. Fluids* **15**, 2141–2151.

Sipp, D. 2012 Open-loop control of cavity oscillations with harmonic forcings. *J. Fluid Mech.* **708**, 439–468.

Sipp, D. & Jacquin, L. 2000 Three-dimensional centrifugal-type instabilities of two-dimensional flows in rotating systems. *Phys. Fluids* **12**, 1740–1748.

Sipp, D., Lauga, E. & Jacquin, L. 1999 Vortices in rotating systems: Centrifugal, elliptic and hyperbolic type instabilities. *Phys. Fluids* **11**, 3716–3728.

Sipp, D. & Lebedev, A. 2007 Global stability of base and mean flows: a general approach and its applications to cylinder and open cavity flows. *J. Fluid Mech.* **593**, 333–358.

Theofilis, V. 2000 Globally unstable basic flows in open cavities. *AIAA Paper 00-1965* .

de Vicente, J., Basley, J., Meseguer-Garrido, F., Soria, J. & Theofilis, V. 2014 Three-dimensional instabilities over a rectangular open cavity: from linear stability analysis to experimentation. *J. Fluid Mech.* **748**, 189–220.

Yamouni, S., Sipp, D. & Jacquin, L. 2013 Interaction between feedback aeroacoustic and acoustic resonance mechanisms in a cavity flow: a global stability analysis. *J. Fluid Mech.* **717**, 134–165.